

# Designing an asymmetric ether-like lithium salt to enable fast-cycling high-energy lithium metal batteries

Received: 16 May 2022

Accepted: 23 May 2023

Published online: 22 June 2023



Yingchun Xia<sup>1</sup>, Pan Zhou<sup>1</sup>, Xian Kong<sup>2,3</sup>, Jiekang Tian<sup>4</sup>, Weili Zhang<sup>1</sup>, Shuaishuai Yan<sup>1</sup>, Wen-hui Hou<sup>1</sup>, Hang-Yu Zhou<sup>1</sup>, Hao Dong<sup>1</sup>, Xiaoxia Chen<sup>1</sup>, Peican Wang<sup>1</sup>, Ziang Xu<sup>1</sup>, Lei Wan<sup>1</sup>, Baoguo Wang<sup>1</sup> & Kai Liu<sup>1</sup>✉

Conventional carbonate-based electrolytes with high corrosion towards Li metal result in massive dendrite growth and limited cycling life, particularly true for practical Li-metal batteries with high cathode loading ( $>3.5 \text{ mAh cm}^{-2}$ ). Herein we design an asymmetric Li salt, lithium 1,1,1-trifluoro-*N*-[2-[2-(2-methoxyethoxy)ethoxy]ethyl]methanesulfonamide (LiFEA) that possesses a pseudo-crown ether-like, folded molecular geometry. It enables carbonate electrolytes with a large apparent donor number and  $\text{Li}^+$  transference number and drives a self-cleaning mechanism for solid–electrolyte interphases, enhancing compatibility with Li-metal anodes even at high current densities. LiFEA-based carbonate electrolytes notably improved fast-cycling performances of Li || NCM811 cells. Pouch cells of  $310 \text{ Wh kg}^{-1}$  achieved  $\sim 410 \text{ W kg}^{-1}$  power density at the discharging current density of  $6.59 \text{ mA cm}^{-2}$ . Under fast-cycling conditions (charging:  $1.46 \text{ mA cm}^{-2}$ , discharging:  $3.66 \text{ mA cm}^{-2}$ ), pouch cells maintained 81% capacity after 100 cycles. Our work provides insights into the interplay between the molecular structure of Li salts, their physicochemical properties and electrochemical performances.

As current lithium-ion batteries with graphite are approaching their theoretical energy density limit, lithium (Li) metal batteries (LMBs) have attracted increasing attention due to an urgent demand for high-energy-density batteries. However, the development of LMBs has been plagued by limited cycle life and safety concerns that result from side reactions between Li metal and electrolytes and the formation of unstable or metastable solid–electrolyte interphase (SEI)<sup>1,2</sup> (particularly for carbonate-based electrolytes). It has been well studied that generally, a SEI on a Li-metal anode contains multiple organic (for example,  $\text{ROCO}_2\text{Li}$ ,  $-(\text{CH}_2\text{CH}_2\text{O})_n-$ ) and inorganic species (for example,  $\text{Li}_2\text{CO}_3$ , LiF,

$\text{Li}_2\text{O}$ ). Recent work revealed that a higher degree of swelling happens to organic-rich SEIs derived from commercial carbonate electrolytes (that is, 1 M  $\text{LiPF}_6$  in ethylene carbonate/diethyl carbonate (EC/DEC)) than those derived from four other electrolytes (that is, fluorinated carbonate additive, ether, high-salt concentration and fluorinated ether solvent)<sup>3</sup>. This carbonate electrolyte-derived, low-quality SEI expedited the growth of Li dendrites, SEI cracking and continuous decomposition of electrolytes and exhibited poor electrochemical performance.

Li-metal corrosion is directly associated with electrolyte formulations as the SEI protective layer on anodes results from initial chemical

<sup>1</sup>Department of Chemical Engineering, Tsinghua University, Beijing, China. <sup>2</sup>South China Advanced Institute for Soft Matter Science and Technology, School of Emergent Soft Matter, South China University of Technology, Guangzhou, China. <sup>3</sup>Guangdong Provincial Key Laboratory of Functional and Intelligent Hybrid Materials and Devices, South China University of Technology, Guangzhou, China. <sup>4</sup>Center of Pharmaceutical Technology, School of Pharmaceutical Sciences, Tsinghua University, Beijing, China. ✉e-mail: [liukai2019@tsinghua.edu.cn](mailto:liukai2019@tsinghua.edu.cn)

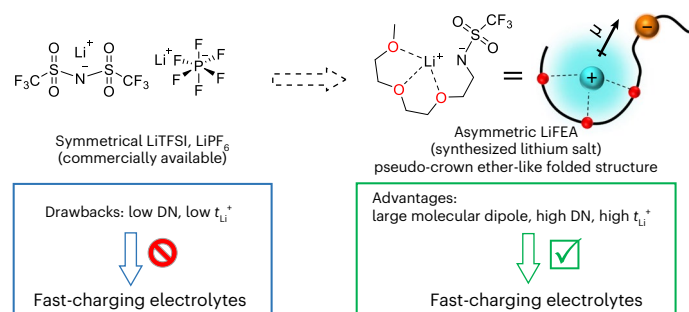


**Fig. 1 | Design principle of LiFEA.** Chemical structures and drawbacks/advantages of commercial, symmetrical Li salts and our synthesized LiFEA with a pseudo-crown ether-like folded structure in carbonate electrolytes. The molecular properties of LiFEA offer notable advantages for developing fast-charging LMBs with carbonate electrolytes.

reactions of Li metal/electrolytes and repeated electrochemical reduction of electrolytes<sup>4–7</sup>. Various electrolyte engineering approaches have been proposed to enhance cyclability, including mixing different commercial solvents/salts<sup>8–11</sup>, optimizing the component ratio<sup>12,13</sup>, combining multiple additives<sup>14,15</sup>, developing novel liquefied gas electrolytes<sup>16</sup>, using (localized) high-concentration electrolytes<sup>17–19</sup> and designing new solvents or salts<sup>20,21</sup>. All these tactics follow a presumption that building inorganic-rich, high-quality SEIs coated on Li metal enhances the mechanical strength of SEIs and facilitates uniform Li plating, thus improving electrochemical performance. Although these approaches made substantial achievements, current LMBs are still far from the requirements of practical applications. Under practical conditions, LMBs are assembled with high-loading cathode active materials (>3.5 mAh cm<sup>−2</sup>), limited Li excess and cycled-in lean electrolytes (<3 g Ah<sup>−1</sup>) (ref. 22). These harsh requirements accelerate dendrite growth, electrolyte depletion and final cell failure, particularly at high operating current densities (>1 mA cm<sup>−2</sup>) for acceptable charging/discharging rates. Therefore, it is urgently demanded to develop new strategies to enrich the toolbox of building a robust, more inorganic-rich and uniform SEI against long cycling under these harsh practical conditions.

In this work, we synthesized an asymmetric functional Li salt, lithium 1,1,1-trifluoro-*N*-(2-[2-(2-methoxyethoxy)ethoxy]ethyl) methanesulfonamide (LiFEA, Fig. 1), which is derived from commercialized lithium bis(trifluoromethanesulfonyl)imide (LiTFSI) by substituting a trifluoromethanesulfonyl unit (CF<sub>3</sub>SO<sub>2</sub>) with an ethylene glycol-based chain. Our designed LiFEA drives Li<sup>+</sup> dissociation from the sulfonyl oxygen atoms to electron-donating ether moiety, presenting a pseudo-crown ether-like binding geometry. Unlike traditional Li salts, LiFEA possesses positively charged ether moieties and negatively charged CF<sub>3</sub>SO<sub>2</sub>N<sup>−</sup> domains, resembling the structure of zwitterions. It has a large dipole moment and high donor number (DN) and can heighten the Li<sup>+</sup> transference number ( $t_{\text{Li}^+}$ ) of carbonate-based electrolytes when used as additives. Furthermore, LiFEA owns a self-cleaning mechanism: cleaning out some undesirable organic species in SEIs and gradually enriching the inorganic species. With these outstanding merits, LiFEA-based carbonate electrolytes notably improve the morphology of deposited Li metal, rate capability and fast-cycling life of Li || NCM811 cells. For practical Li-metal pouch cells, LiFEA-based electrolytes enabled a high specific energy density of up to 310 Wh kg<sup>−1</sup> and a discharging power density of 410 W kg<sup>−1</sup>. Under fast-cycling conditions (charging: 1.46 mA cm<sup>−2</sup>, discharging: 3.66 mA cm<sup>−2</sup>), pouch cells retained 81% capacity after 100 cycles.

## Molecular design and characterization

Commercial Li salts with a symmetrical molecular geometry (for example, LiPF<sub>6</sub>, LiTFSI) have high ionic conductivities but low  $t_{\text{Li}^+}$

(typically < 0.3). It is generally accepted that the migration of Li<sup>+</sup> determines the rate capability of LMBs, however, moved anions yield concentration polarization to induce an impedance increase and drastic capacity drop at high operating current densities, particularly for carbonated-based electrolytes<sup>23,24</sup>. Moreover, carbonate electrolytes using these conventional Li salts will result in an organic-rich SEI, which is harmful to LMB performance. To address these issues, we hypothesized that an asymmetric, large molecular dipole Li salt—designed by incorporating an electron-withdrawing group and electron-donating moiety into the anion to heighten  $t_{\text{Li}^+}$ —could lead to the formation of a high-quality SEI/cathode-electrolyte interface (CEI). First, we retained one of the strong electron-withdrawing CF<sub>3</sub>SO<sub>2</sub> groups and its linked nitrogen atom in LiTFSI to delocalize the negative charge<sup>25,26</sup>. Second, an ether backbone was introduced because of its electron-donating ability<sup>27</sup> to capture the migrated Li<sup>+</sup>. The resultant Li salt shows a folded molecular geometry, similar to the Li<sup>+</sup>-(pseudo) crown ether supramolecular complex, endowing the LiFEA with a larger molecular dipole moment, DN and  $t_{\text{Li}^+}$  due to the intramolecular zwitterion-like property.

We first identified the product of LiFEA by multiple characterizations after synthesis (Supplementary Figs. 1–4) and then determined its physicochemical properties. LiFEA has good thermal stability with a melting temperature of −131 °C and a decomposition temperature of −254 °C (Supplementary Fig. 5). Variable-temperature nuclear magnetic resonance spectroscopy is further taken to acquire its molecular structural information in the carbonate solvent (that is, EC/DEC, v/v = 1:1) (Fig. 2a–c). Upon heating, both upfield- and downfield-shifted signals were observed in the LiFEA regions of <sup>1</sup>H nuclear magnetic resonance (NMR) spectra (Fig. 2a,b). Downfield-shifted peaks of the a and d protons indicated more deshielded hydrogen nuclei due to elevated temperature resulting in increased thermal motions and the lengthened distance<sup>28</sup> between Li<sup>+</sup> and O, which is consent with the tendency of Li signals (Fig. 2c). Unexpectedly, peaks ascribed to the g, e and f protons showed an opposite change, upfield-shifted resonances, with the largest shift for the g proton. This result could be rationalized by the more flexible, unfolded C-terminus part promoting more Li<sup>+</sup> interacting with terminal oxygens and holding an overwhelming advantage over other conformations. By a sample cooling test, these changes in chemical shifts disappeared (Supplementary Fig. 6), disclosing molecular information as follows. First, LiFEA emerges as a folded structure at room temperature, as shown in the inset of Fig. 2b. Second, with a heating/cooling treatment, LiFEA shows a reversible conformational change (Supplementary Fig. 6c). This temperature-responsive reversible conformation change demonstrates the non-covalent-bonding nature of the Li<sup>+</sup>-(pseudo) crown ether interaction. Additionally, introducing Na<sup>+</sup> as a competing cation would break its folding structure and enable oxygens neighbouring the C-terminus to bind with more metal ions (Supplementary Fig. 7), offering more robust evidence of LiFEA with a pseudo-crown ether-like folded structure due to intramolecular Li<sup>+</sup> complexation.

To gain further information about the Li–O coordination of LiFEA, we carried out density-functional theory (DFT) and MD simulations. DFT results showed that strong Li–O coordinating ability and high binding energy between Li<sup>+</sup> and FEA anion drive the folded structure of LiFEA and contribute to a relatively stable interaction between Li<sup>+</sup> and the ether domain (Fig. 2d–f and Supplementary Note 1). Because DFT calculations were done in a vacuum state, we conducted MD simulations of 0.1 M LiFEA in EC/DEC (v/v = 1:1) to show that the coordination structure predicted by DFT calculations is relevant in bulk electrolytes. Figure 2g offers a representative snapshot of the Li<sup>+</sup> solvation structure with the most probable compositions in the first solvation shell by FEA, in which oxygens from the ether chain (O<sub>e</sub>) participate actively in the Li<sup>+</sup> solvation. The radial distribution functions of both Li–O<sub>e</sub> and Li–O<sub>s</sub> indicated that O<sub>e</sub> dominantly contributed to the Li<sup>+</sup> solvation (O<sub>s</sub> refers to oxygen atoms from the FEA head) (Fig. 2h).

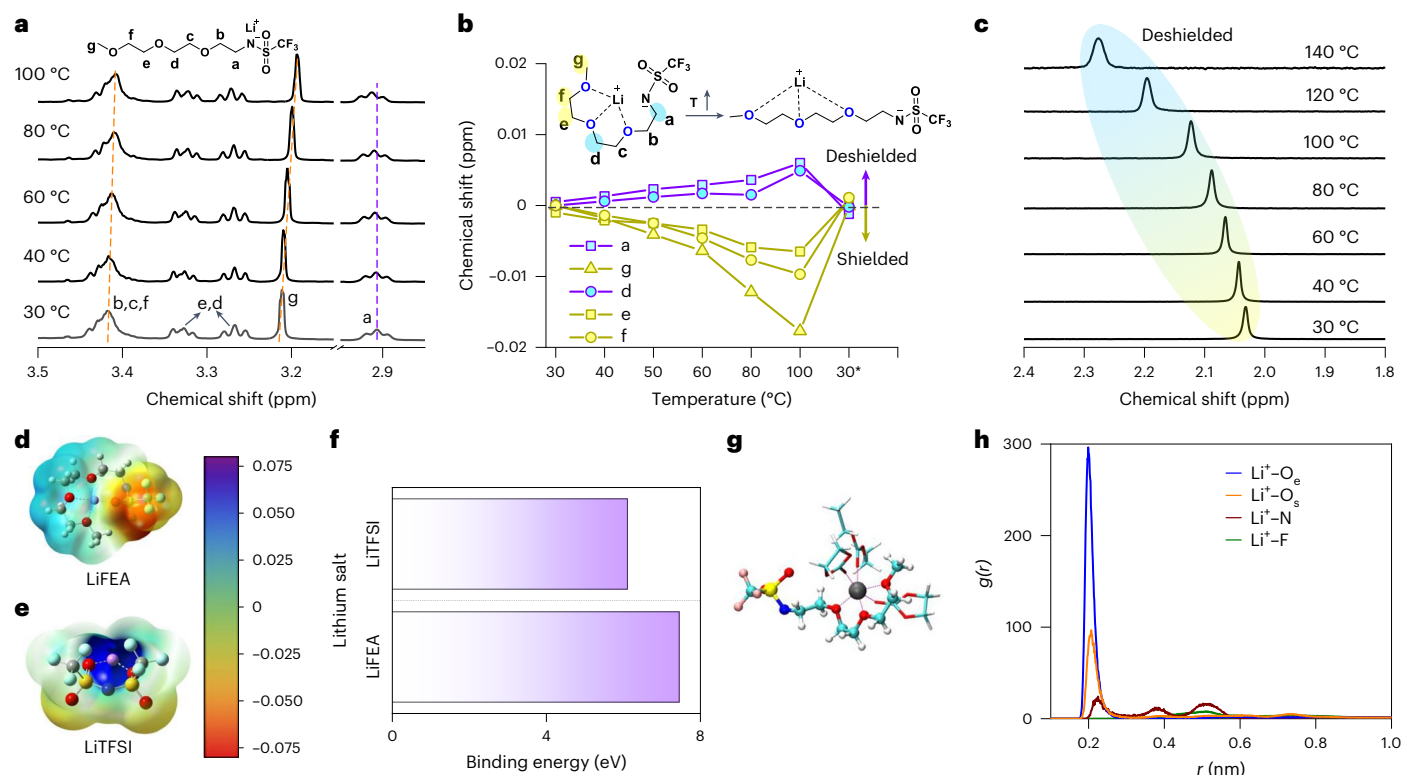


**Fig. 2 | Experimental and theoretical study on pseudo-crown ether-like folded structure of LiFEA. a–c,** Variable-temperature nuclear magnetic resonance spectra for varied geometry of LiFEA upon heating: stacked  $^1\text{H}$  NMR (a), changed chemical shifts of typical peaks based on the chemical shifts at 30 °C (b) and stacked  $^7\text{Li}$  NMR (c). Note that the x-axis break aims to provide an enlarged view of the LiFEA proton peaks. The asterisk (\*) indicates the cooling temperature after heating. The NMR sample tube was equipped with a coaxial

tube for DMSO- $d_6$ . **d–f,** DFT calculations for LiFEA: ESP distribution of LiFEA (d) and LiTFSI (e); binding energy between  $\text{Li}^+$  and anion part for LiFEA and LiTFSI (f). **g, h,** Solvation structure of LiFEA in EC/DEC (v/v = 1:1): the most probable solvated structure of LiFEA obtained from MD simulations where the LiFEA concentration is 0.1 M (g), the radial distribution functions  $g(r)$  in the centre-of-geometry distance between of  $\text{Li}^+$  and investigated atoms (h).

## Advantages of high donor number and $\text{Li}^+$ transference number

LiFEA featuring a pseudo-crown ether-like molecular geometry inherently possesses a large molecular dipole moment (Supplementary Fig. 8), inspiring some advantages as an electrolyte component. The total interactions between LiFEA and acceptor are evaluated by the DN parameter, which involves contributions from dipole–dipole or dipole–ion interactions, electron-donating ability and even steric properties<sup>29</sup>. We tried to measure DN for FEA anions following the standard  $^{23}\text{Na}$  NMR measurements<sup>30,31</sup>; nevertheless, strong binding interaction between the ether domain and  $\text{Na}^+$  caused a broad peak and large error (Supplementary Fig. 9). Accordingly, we regarded LiFEA and solvent as an entirety to determine the apparent DN of as-prepared solutions (Supplementary Figs. 10–17 and Supplementary Table 1). The DN value increases with the gradual addition of LiFEA to baseline solvents. Specifically, once LiFEA was added to acetonitrile and up to a concentration of 0.1 M, the DN value increased from 14 to 18  $\text{kcal mol}^{-1}$ . Its value further elevated to 22  $\text{kcal mol}^{-1}$  when the concentration of LiFEA increased to 1.0 M (Fig. 3a). The heightened DN stems from molecular features of LiFEA, intrinsically carrying several potential interacting sites for acceptors (for example, ether domain and sulfuryl) and a larger molecular dipole induced by the folded structure of LiFEA. To exclude the interference from other factors, we took LiTFSI as a control and found a negligible change in DN values with an increasing concentration of LiTFSI from 0.1 to 1.0 M. Similar tendencies were observed in a binary solvent system of EC and DEC (Fig. 3b), indicating that LiFEA could efficiently modulate DN of the baseline solvents, that is, the electron-donating property and ability to interact with acceptors.

Generally, high-DN electrolytes are expected to promote the solubility of Li salts and organic species<sup>32</sup>, validated by quantitative inductively coupled plasma-optical emission spectrometry or NMR analysis. Figure 3c depicts three typical Li salts in SEIs with extremely low solubility in the carbonate solvent. In contrast, they showed increased solubility up to at least 10–40 times with the help of 0.1 M LiFEA. More importantly, the enhanced solubility of a well-known  $\text{LiNO}_3$  additive for improving Li anode performance was above 309% of its initial value, which would enrich the formulation of LiFEA-based electrolytes. In addition to inorganic salts, LiFEA could also be a solubility enhancer for organic Li salts and polymeric species (Supplementary Fig. 18 and Supplementary Table 2). Benefitting from the increased solubility induced by LiFEA, as demonstrated later, LiFEA in electrolytes could promote the dissolution of undesirable Li salts/organic species out of an SEI, eventually leading to a compact and inorganic-rich SEI. On the other hand, the molecular feature of LiFEA surprisingly created an outstandingly high  $t_{\text{Li}^+}$  value of 0.78 (Fig. 3d and Supplementary Fig. 19). Despite  $\text{LiPF}_6$  showing a low  $t_{\text{Li}^+}$  in the commercial carbonate electrolyte, introducing an additive level of LiFEA (0.1 M) could effectively heighten a  $t_{\text{Li}^+}$  value from 0.16 to 0.47 (Supplementary Figs. 20 and 21), endowing carbonate electrolytes with a potential superior rate capability.

## Fast-cycling carbonate electrolytes

Highlighted advantages of LiFEA motivated us to assess the electrochemical performances of LiFEA-based carbonate electrolytes by Li | NCM811 batteries. To systematically explore the role of LiFEA in carbonate electrolytes, we utilized three electrolytes for the battery cycling test: commercial electrolyte, 1.0 M  $\text{LiPF}_6$  in EC/DEC (v/v = 1:1)

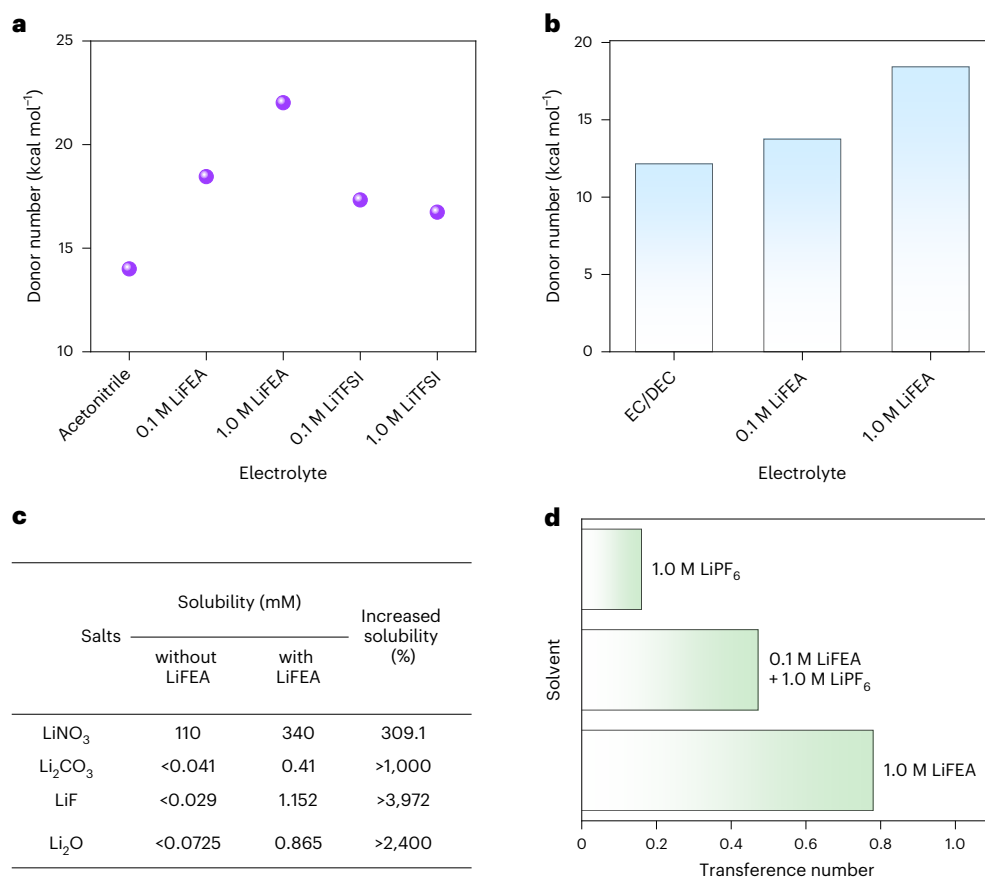


**Fig. 3 | Physicochemical properties of LiFEA and LiFEA-based electrolytes. a, b,** Determination of apparent DN: LiFEA dissolved in acetonitrile (**a**) and binary solvent of EC/DEC (v/v = 1:1) (**b**). **c,** Comparison of the solubility of Li salts in the presence and absence of LiFEA in EC/DEC (v/v = 1:1). **d,** LiFEA-mediated high Li<sup>+</sup> transference number ( $t_{Li^+}$ ) for EC/DEC (v/v = 1:1).

as a reference carbonate electrolyte (note as RCE), LiFEA electrolyte (prepared by adding 0.1 M LiFEA into RCE) used to figure out the effects of LiFEA itself on LMBs and advanced LiFEA electrolyte (prepared by dissolving 0.1 M LiNO<sub>3</sub> and 0.1 M LiFEA additives into RCE) used to fully exploit the potential advantage of LiFEA and evaluate the advanced performance of LiFEA-based electrolytes.

We used thick Li metals and moderate loading cathodes (active materials: ~3 mg cm<sup>-2</sup>) to evaluate the intrinsic battery performance of designed electrolytes. In the rate capability test, cells with LiFEA electrolyte showed a superb rate capability (Fig. 4a and Supplementary Fig. 22), with a specific capacity of ~195 and 166 mAh g<sup>-1</sup> at 0.2 and 2 C, respectively. When the cycling rate increased to 5 and 10 C, the specific capacity remained at ~143 and 110 mAh g<sup>-1</sup>, respectively. In contrast, RCE offered a low specific capacity of ~190, 160 and 120 mAh g<sup>-1</sup> at 0.2, 2 and 5 C, respectively. A rapid capacity loss occurred at 10 C with a limited capacity of ~50 mAh g<sup>-1</sup>, resulting from low Coulombic efficiency and increased overpotential. The improved capacity retention of LiFEA electrolytes supported that LiFEA has great potential to boost carbonate electrolytes' fast-cycling performance. Furthermore, advanced LiFEA electrolytes showed a lower capacity loss from 0.2 to 10 C rate than LiFEA electrolytes, with a high discharge capacity of ~190, 180, 165 and 133 mAh g<sup>-1</sup> at 1, 2, 5 and 10 C (Fig. 4a), respectively. These results revealed that advanced LiFEA electrolytes endowed LMBs with more excellent rate capability than LiFEA electrolytes because of the contribution of dissolved LiNO<sub>3</sub>. Given that advanced LiFEA electrolytes possess the most outstanding rate capability among the designed electrolytes, we will discuss it in more detail in the following battery tests and take LiFEA electrolytes to elucidate the LiFEA salt's role in battery performance if it is necessary.

The cycling stability of advanced LiFEA electrolytes and RCE was evaluated under a high cycling current density (2, 5 C, 1 C = 0.6 mA cm<sup>-2</sup>) (Fig. 4b–d and Supplementary Fig. 23), which is generally thought to be a great challenge for preventing Li corrosion and speedy capacity fade of Li||NCM batteries<sup>10</sup>. The cell operating with RCE exhibited 54.2% capacity retention after 100 cycles at 5 C, caused by continuous capacity fading and overpotential increase during cycling. Despite cycling at 1.2 mA cm<sup>-2</sup> (that is, 2 C), the specific capacity of cells still dropped abruptly, maintaining 79.1% capacity after 80 cycles. In sharp contrast, advanced LiFEA electrolytes enabled an extended cycle life and higher capacity retention under identical conditions. The cell operating at 2 C retained its 81.5% capacity after 480 cycles. At 5 C, advanced LiFEA electrolyte delivered a high specific capacity of 141 mAh g<sup>-1</sup> at the 500th cycle with 83.5% capacity retention, effectively overcoming the increase of cell overpotential (Fig. 4b,d). The distinguished long-term cycling stability and fast-cycling behaviours inferred that the bulk electrolyte and SEI/CEI layers derived from advanced LiFEA electrolytes promoted Li<sup>+</sup> transportation compared to RCE (Supplementary Figs. 24–26, Supplementary Table 3 and Supplementary Note 2).

We further evaluated the electrochemical performance of full cells with 40 μm Li foils and high-loading cathodes (2.6 mAh cm<sup>-2</sup>). Advanced LiFEA electrolytes provided a high discharge capacity of ~200 mAh g<sup>-1</sup> during three formation cycles at 0.1 C and 97.3% capacity retention after 150 cycles at 1 C, showing an outstanding average Coulombic efficiency of >99.1% (Supplementary Fig. 27). Notably, the battery operated for more than 100 cycles with a capacity retention of 86.5% at 2 C (that is, 5.2 mA cm<sup>-2</sup>) (Fig. 4e), due to its robust SEI/CEI layer with fast Li<sup>+</sup> transport. In comparison, batteries tested in RCE deteriorated quickly after ~30 cycles at these high current densities.



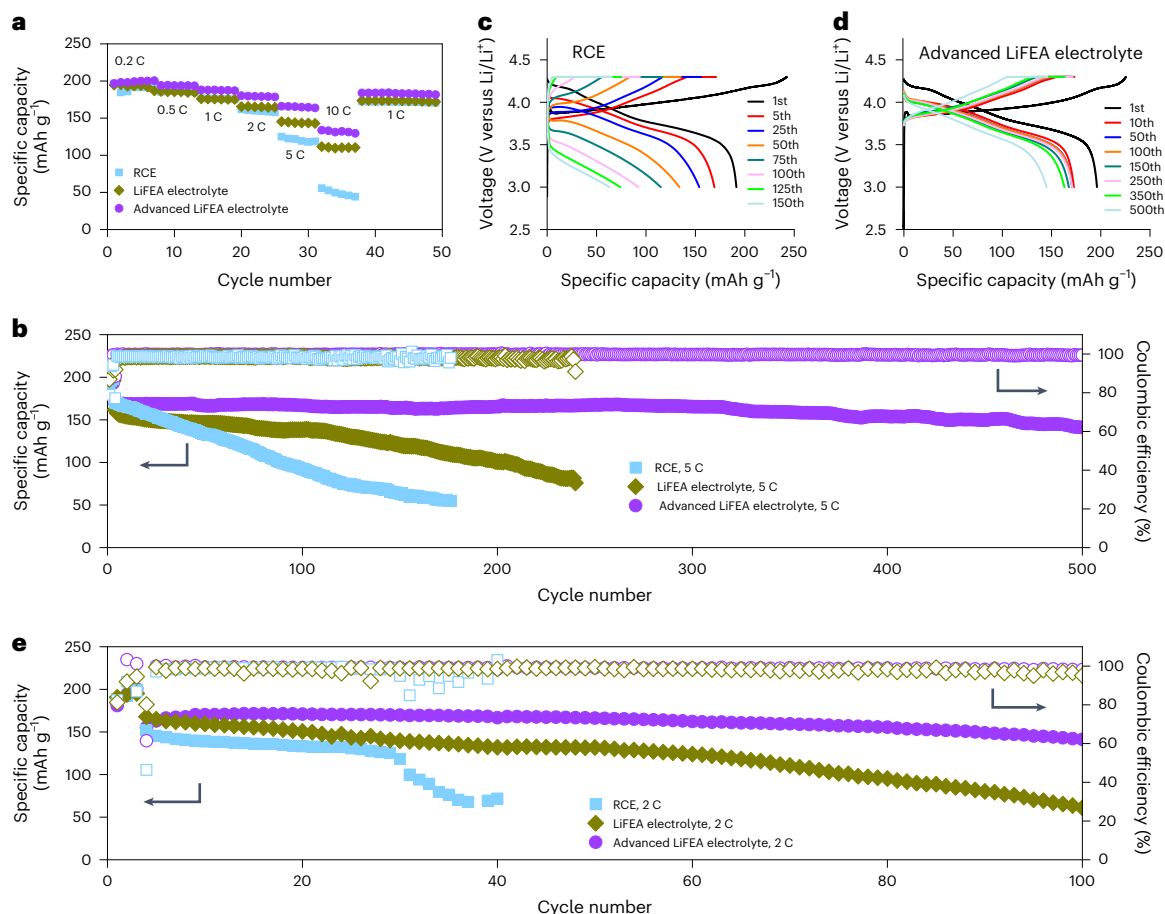


**Fig. 4 | Electrochemical performance of Li | NCM811 batteries. a,b,** Rate performance and long-term cycling with RCE, LiFEA electrolyte and advanced LiFEA electrolyte. **c,d,** Typical charge/discharge curves as a function of cycle number using electrolytes of RCE and advanced LiFEA electrolyte. The cells were

charged and discharged between 3 and 4.3 V at a rate of 5 C (that is, 3 mA cm<sup>-2</sup>).

**e,** Full cell with thin Li foils and high loading NCM811 active materials at a constant charging/discharging current density of -5.2 mA cm<sup>-2</sup> (that is, 2 C) after three formation cycles at 0.1 C.

The differences in full-cell performance showed that the additives in advanced LiFEA electrolytes were crucial for enhancing the fast-cycling stability of RCE. Additionally, we did systematic studies to confirm that the molecular structure of LiFEA played a decisive role in the fast-cycling properties of LiFEA-based electrolytes (Supplementary Figs. 28 and 29 and Supplementary Note 3).

## Performance of practical Li-metal pouch cells

The superior rate performance and long cycling stability make advanced LiFEA electrolytes promising for practical LMBs. Pouch cells paired with 50-μm-thick Li foils (~10 mAh cm<sup>-2</sup>) and high-loading NCM811 (~3.66 mAh cm<sup>-2</sup>) offered an N/P ratio of 2.7 and cycled under a lean electrolyte condition (E/C = 2.8 g Ah<sup>-1</sup>), allowing an initial specific energy density of ~310 Wh kg<sup>-1</sup>. This value was up to ~413 Wh kg<sup>-1</sup>, excluding the mass of taps and packing foil, which could be a valuable parameter for evaluating the energy density of larger size batteries. To determine a limiting current density of advanced LiFEA electrolytes, we first assessed performances of rate capability with two different protocols: charging/discharging at the same current density, constant charging at 1.46 mA cm<sup>-2</sup> and increasing discharging rate. Under two different protocols, advanced LiFEA electrolytes presented excellent fast-cycling capability compared to RCE (Fig. 5a,b). For pouch cells in RCE, a sudden capacity drop started with cycling at 3.66 mA cm<sup>-2</sup> and cells operated worse in the following extended cycles. Surprisingly, advanced LiFEA electrolytes endowed pouch cells with superior cycling stability and high capacity even at a large discharging current density

of 6.59 mA cm<sup>-2</sup>, and their corresponding power densities were shown in Fig. 5c. The maximum power density was calculated to be ~410 W kg<sup>-1</sup> (except taps and packing foil: ~550 W kg<sup>-1</sup>) at 6.59 mA cm<sup>-2</sup> for advanced LiFEA electrolytes; contrastingly, RCE enabled a maximum value of ~320 W kg<sup>-1</sup> (except taps and packing foil: ~425 W kg<sup>-1</sup>) at 5.12 mA cm<sup>-2</sup>. It should be noted that it is tough for practical Li-metal pouch cells to simultaneously achieve a high energy and power density since the development of charging/discharging current density is slow and still far from satisfactory for LMB practical applications<sup>33</sup>. For commercial LiPF<sub>6</sub>/carbonate electrolytes, fast charging current density at >0.6–0.7 mA cm<sup>-2</sup> (comparable to only 0.17–0.2 C rate for 3.5 mAh cm<sup>-2</sup> cathodes) is already particularly harmful to LMBs due to hazardous Li dendrites and continuous growth of SEI<sup>22</sup>. Combined with the power density and energy density of advanced LiFEA electrolytes, our results show the best comprehensive property to our knowledge in the realm of LMBs from aspects of both the high charging and discharging rates (Fig. 5d, Supplementary Figs. 30 and 31 and Supplementary Table 4).

Moreover, we tested the long cycling stability of advanced LiFEA electrolytes. As shown in Fig. 5e, cells delivered a total capacity of 400 mAh and maintained 90% capacity retention after 120 cycles with a slow-charging rate of 0.73 mA cm<sup>-2</sup> and a fast-discharging rate of 2.20 mA cm<sup>-2</sup>. In contrast, cells with RCE survived only 25 cycles under identical conditions. The extending cycle life indicated that advanced LiFEA electrolytes contributed to fast Li<sup>+</sup> transportation under stringent conditions. Under a higher cycling current density, advanced LiFEA electrolyte still enabled a high reversible Li<sup>+</sup> plating/stripping,

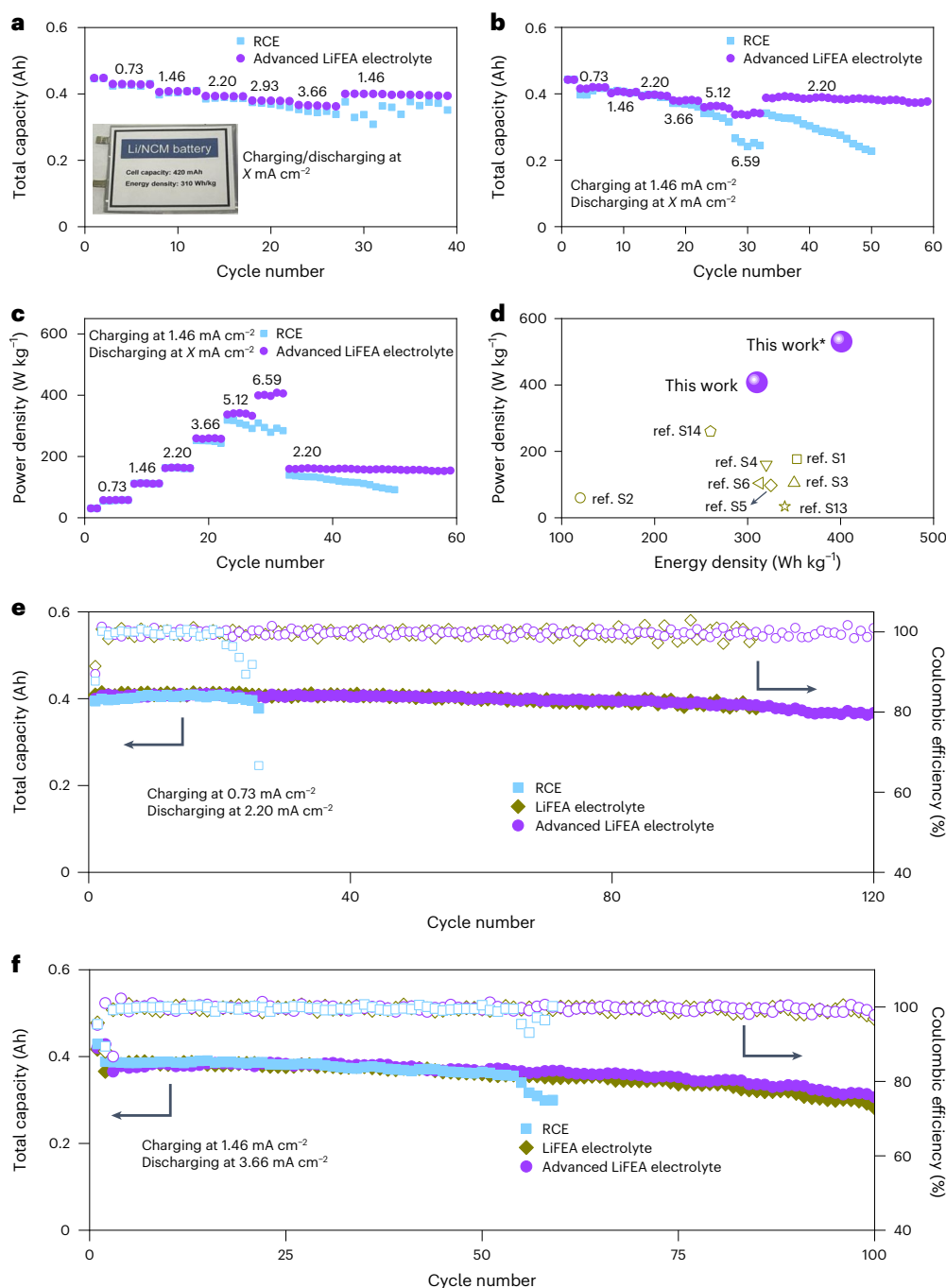


**Fig. 5 | Performance of Li | NCM811 pouch cells under stringent conditions.**

**a,b**, Rate performance: charging/discharging at the same current density (**a**); charging at  $1.46 \text{ mA cm}^{-2}$  but discharging at an increasing current density (**b**). Inset: an image of the pouch cell. **c**, Power density under different discharging current densities. **d**, Comparison of a cell-level (output) energy density and power density with state-of-the-art electrolytes/strategies. 'Ref. Sx' represents

Supplementary reference x. The asterisk (\*) indicates an energy density and power density without counting the mass of taps and packing foil. **e**, Long cycling stability at  $0.73 \text{ mA cm}^{-2}$  charge and  $2.20 \text{ mA cm}^{-2}$  discharge. **f**, Fast charging/discharging performance. Charge:  $1.46 \text{ mA cm}^{-2}$ , discharge:  $3.66 \text{ mA cm}^{-2}$ . All the cycled pouch cells meet the parameters: an N/P ratio of 2.7, an E/C ratio of  $2.8 \text{ g Ah}^{-1}$  and an areal capacity of  $3.66 \text{ mAh cm}^{-2}$ .

with an 86% capacity retention after 100 cycles at  $1.46 \text{ mA cm}^{-2}$  for charging and  $2.93 \text{ mA cm}^{-2}$  for discharging (Supplementary Fig. 32). To achieve special battery applications, we tested the fast-discharging capability at  $3.66 \text{ mA cm}^{-2}$  (Fig. 5f). Cells with advanced LiFEA electrolytes preserved 81% capacity after 100 cycles, but an abrupt fade in both capacity and Coulombic efficiency happened to RCE after ~50 cycles. For another comparison, we surprisingly found that LiFEA electrolytes showed comparable cycling performances to advanced LiFEA electrolytes under identical conditions (Fig. 5e,f and

Supplementary Fig. 33), reflecting that LiFEA worked for fast cycling, but  $\text{LiNO}_3$  did little. The outstanding performance of fast operation enriched LiFEA-based electrolytes as one of the state-of-the-art electrolytes for high-power-density electric devices.

### Li-metal morphology and reversible plating/stripping

In addition to stabilizing NCM811 cathodes, LiFEA enabled the highly reversible Li-metal anode in carbonate electrolytes. Generally, dendrite

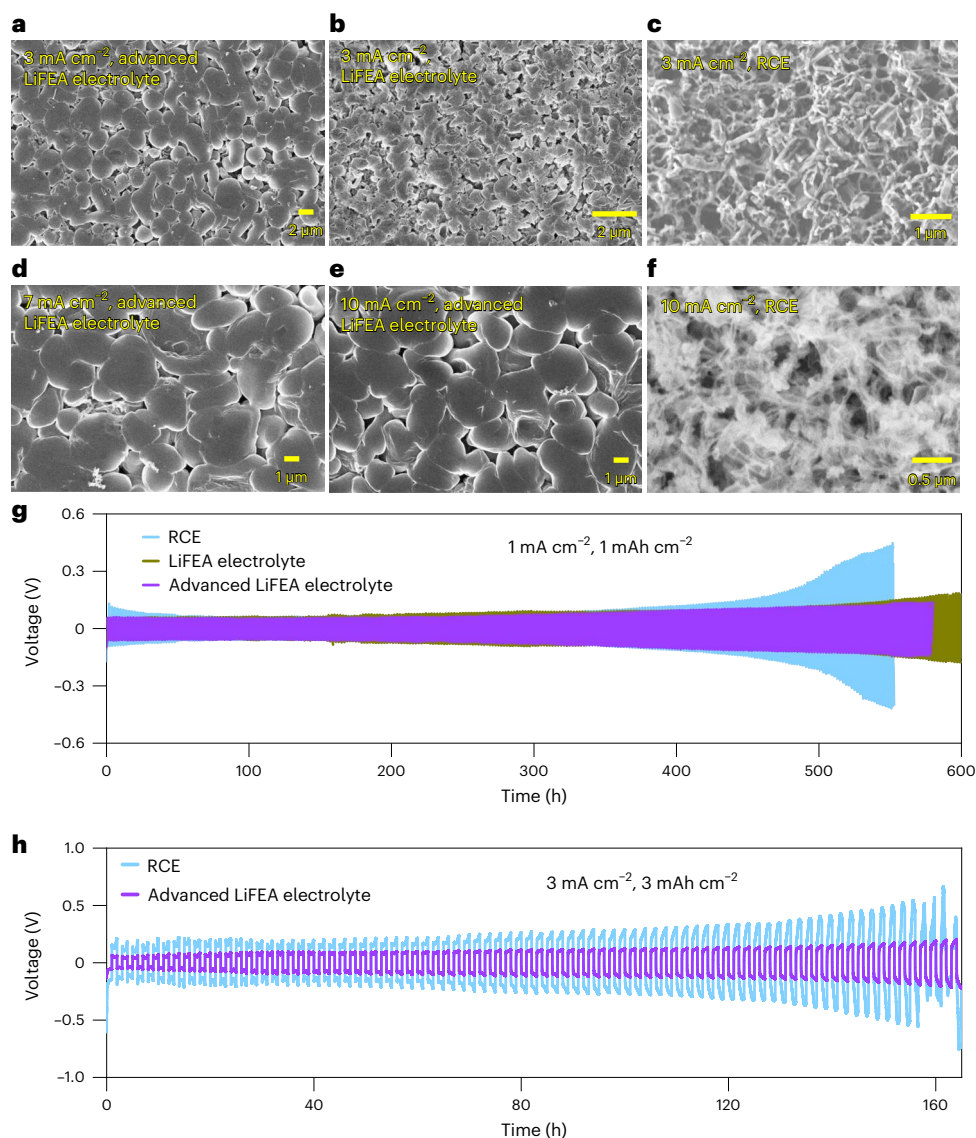


**Fig. 6 | Dendrite-free Li-deposited morphologies and plating/stripping reversibility under high current densities.** **a–c**, SEM images of the deposited Li-metal morphology after cycling in advanced LiFEA electrolytes (**a**), LiFEA electrolytes (**b**) and RCE (**c**) at charging/discharging current densities of 3 mA cm<sup>-2</sup>. **d,e**, SEM images of Li-metal morphologies formed in advanced LiFEA electrolytes at 7 mA cm<sup>-2</sup> (**d**) and 10 mA cm<sup>-2</sup> (**e**). **f**, SEM image of fibre-like Li

dendritic deposition after cycling in RCE at 10 mA cm<sup>-2</sup>. **g**, Reversible Li plating/stripping in Li || Li symmetric cells with advanced LiFEA electrolytes, LiFEA electrolytes and RCE under current densities of 1 mA cm<sup>-2</sup>. **h**, Comparison Li plating/stripping performance with Li || Li symmetric cells cycling in advanced LiFEA electrolytes and RCE at 3 mA cm<sup>-2</sup>, 3 mAh cm<sup>-2</sup>. The area capacity was 1 mAh cm<sup>-2</sup> in **a–f**.

growth is a critical factor in the capacity loss and short circuit of LMBs at high charging/discharging current densities<sup>34</sup>. To investigate Li anode performance, we observed the morphological evolution of Li metal in different electrolytes by ex situ scanning electron microscopy (SEM). Instead of growing into dendrites in RCE, granular Li-metal particles uniformly distributed on Cu substrates in the presence of LiFEA-based electrolytes (that is, advanced LiFEA electrolytes and LiFEA electrolytes) (Fig. 6a–f). In detail, the compact aggregates of Li particles generated in advanced LiFEA electrolytes showed an immensely larger size than LiFEA electrolytes at 3 mA cm<sup>-2</sup>. When the current density increased to 7 mA cm<sup>-2</sup>, this Li morphology evolved into densely packed spherical Li with a diameter of ~3 μm. Interestingly, such Li-deposited shapes remained well until the current density increased to as high as 10 mA cm<sup>-2</sup> (Fig. 6e). However, for RCE, severe needle-like dendrites grew at 3 mA cm<sup>-2</sup> and transformed into fibrous Li with a highly porous structure at 10 mA cm<sup>-2</sup> (Fig. 6c,f), indicating detrimental side reactions between the bulk Li and fresh electrolyte caused by inferior SEIs<sup>6</sup>. These

phenomena validated that LiFEA contributed a uniform Li<sup>+</sup> plating/stripping at high current densities, and the dissolved LiNO<sub>3</sub> further enhanced a more reversible Li deposition.

The reversible Li<sup>+</sup> plating/stripping was further corroborated by Li || Li symmetric cells. Cells with RCE showed a vast increase in overpotentials and short cycling life at high current densities (1, 2, 3 mA cm<sup>-2</sup>) (Fig. 6g,h and Supplementary Fig. 34). In comparison, advanced LiFEA electrolytes and LiFEA electrolytes experienced lower overpotentials and had longer lifespans. The excellent maintenance of low overpotentials in LiFEA-based electrolytes verified that LiFEA enabled fast Li<sup>+</sup> migration and superior SEI properties, reflected by the high-performance, fast-cycling capability of LMBs.

### Self-cleaning SEI by the LiFEA-based electrolyte

As previously reported, many factors limit the fast-cycling behaviour in batteries<sup>24</sup> such as ionic conductivity, viscosity and wettability of electrolytes,  $t_{\text{Li}^+}$  and the structure and composition of SEI. In addition

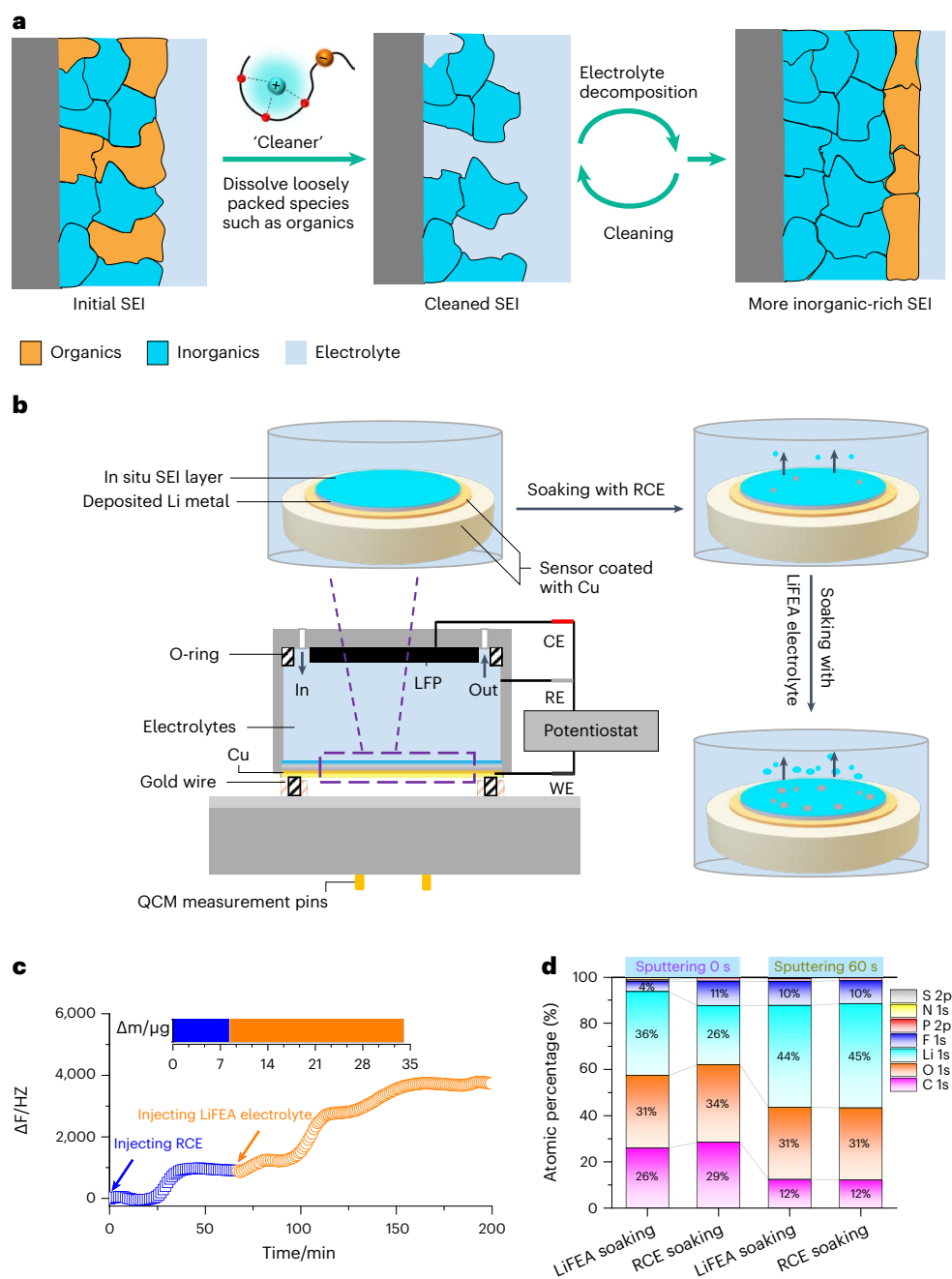


**Fig. 7 | LiFEA self-cleaning concept and results of EC-QCM experiments for SEIs. a**, A proposal for self-cleaning of the SEI mechanism. **b**, Schematic diagram of EC-QCM illustrates that an in situ SEI layer grows on the surface of Li metal deposited on the Q sensor, and the built SEI underwent two-step soaking treatments. Once some SEI components dissolve in electrolytes, the Q sensor will output a higher frequency record from which we can calculate the mass loss according to a formula:  $\Delta m = -C\Delta f/n$ . In this formula,  $\Delta m$  is the mass change of SEI,  $C$  is a constant of  $17.7 \text{ ng Hz}^{-1} \text{ cm}^{-2}$ , indicating the sensitivity factor of the quartz crystal,  $n$  is the overtone of the oscillations ( $n = 3$  for the analyzed data),

and  $\Delta f$  is the resonance frequency change. **c**, The SEI formed in RCE underwent mass loss when it soaked in fresh RCE and LiFEA electrolytes. **d**, SEI composition changes after soaking in LiFEA electrolyte and RCE. The SEIs were formed in RCE after 10 cycles at  $3 \text{ mA cm}^{-2}$ ,  $1 \text{ mAh cm}^{-2}$ . Sputtering 0 s and 60 s represent the  $\text{Ar}^+$  sputtering time during the XPS measurement to study the depth profile of the elemental distribution of the SEI. RE, CE, WE and LFP refer to the reference electrode, counter electrode, working electrode and lithium iron phosphate, respectively.

to the fast  $\text{Li}^+$  transport in LiFEA-based electrolytes (Supplementary Figs. 35 and 36 and Supplementary Note 4), we wonder if there are other mechanisms for such a vast improvement because the increase of  $t_{\text{Li}^+}$  up to  $-0.5$  alone could not fully support such fast charging/discharging capability. It has been well acknowledged that organic-based species are more loosely packed and vulnerable to electrolyte attack than inorganic-based species in the SEI, thus resulting in severe swelling

issues and insufficient electrode protection. Here we hypothesized that LiFEA with a self-cleaning mechanism due to its molecular feature and high-DN property could dissolve the hazardous organic-based species, gradually enrich inorganics and eventually improve the quality of SEIs for fast-cycling capabilities (Fig. 7a).

To gain more insightful information about the evolution process of the SEI induced by LiFEA, we combined quartz crystal microbalance



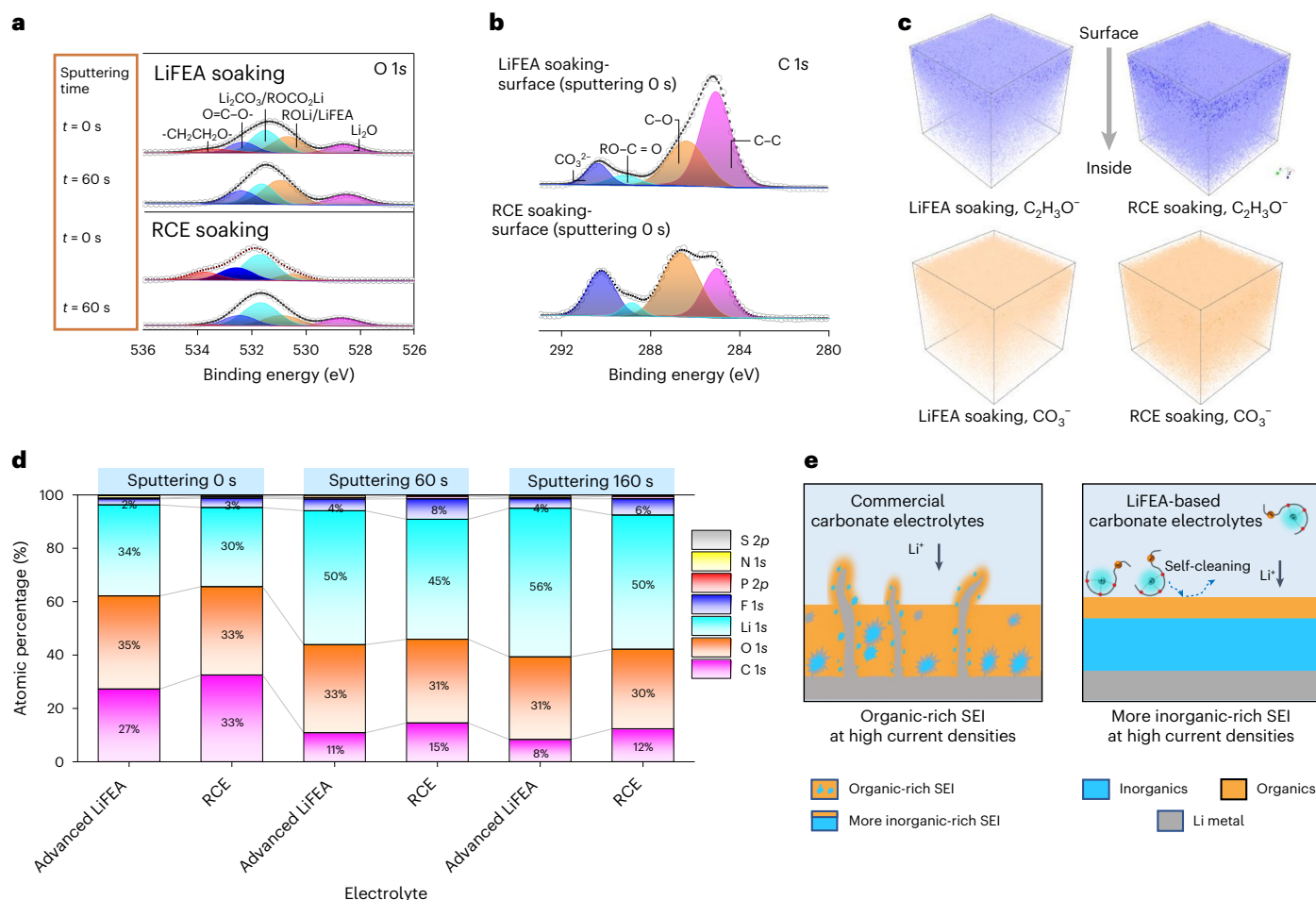


**Fig. 8 | Components of SEIs with different soaking electrolytes and cycling electrolytes. a, b,** O 1s and C 1s XPS spectra of SEIs after soaking with RCE and LiFEA electrolyte (marked as LiFEA in the figure). **c,** TOF-SIMS 3D images of  $\text{C}_2\text{H}_3\text{O}^-$  and  $\text{CO}_3^-$  from soaked SEIs. Maximum intensity: blue colour (orange) and minimum intensity: white. The SEI layers were formed in RCE after ten cycles at  $3 \text{ mA cm}^{-2}$ ,  $1 \text{ mAh cm}^{-2}$ , washed by DEC and finally soaked with RCE or LiFEA electrolyte for two days before the ex situ analysis (a–c). **d,** Difference in

elemental compositions of SEIs formed in advanced LiFEA electrolytes (marked as advanced LiFEA in the figure) and RCE, measured by XPS analysis. Cycling at  $3 \text{ mA cm}^{-2}$ ,  $1 \text{ mAh cm}^{-2}$  for ten cycles and without further soaking. Sputtering 0 s, 60 s and 160 s represent the sputtering time using  $\text{Ar}^+$ , and 0 s refers to the top surface of the SEI. **e,** LiFEA-based electrolytes enabling a more inorganic-rich SEI layer and dendrite-free Li deposition by self-cleaning action, compared with commercial carbonate electrolytes.

analysis with electrochemical methods (EC-QCM) to track changes in the SEI film mass during soaking treatment<sup>35</sup> (Supplementary Fig. 37). The design principle of EC-QCM experiments were shown in Fig. 7b (Supplementary Note 5). After the pristine SEI was soaked with RCE, the Q sensor accessed a balance stage within 40 min, and the resonance frequency change ( $\Delta f$ ) increased to 916.0 Hz, indicating that the SEI film experienced a mass loss of 8.3  $\mu\text{g}$  (Fig. 7c). During the residue SEI soaking with LiFEA electrolyte, the Q sensor underwent a remarkable frequency shift and took longer to recover balance. The decreased mass of SEI was 25.7  $\mu\text{g}$ , three times higher than that of RCE (Fig. 7c inset).

X-ray photoelectron spectroscopy (XPS) analysis further identified the lost (dissolved) components of SEIs after the soaking treatment. The residue SEI after soaking with LiFEA electrolyte contained higher Li content but slightly lower C, O and F atomic ratios on its surface than that of RCE (Fig. 7d). By XPS analyses of O 1s, C 1s and F 1s spectra, the dissolved organic-based species were proven to be  $-(\text{CH}_2\text{CH}_2\text{O})_n-$ , carbonates (for example,  $\text{ROCO}_2\text{Li}$ )<sup>10,16,36</sup> (Fig. 8a,b), and the cleaned F-based species were LiF (Supplementary Fig. 38). A quantitative comparison of these carbonate contents in soaked SEIs made LiFEA's capability of cleaning organic carbonates out of the SEI more apparent (Supplementary Fig. 39). More direct evidence for

this differentiated SEI composition was provided by time-of-flight secondary-ion mass spectrometry (TOF-SIMS) (Supplementary Fig. 40). In TOF-SIMS depth profiles of  $\text{C}_2\text{H}_3\text{O}^-$ , the signal from SEI soaked with LiFEA electrolyte arrived at its maximum normalized intensity earlier than RCE and experienced a steep drop afterwards, indicating that LiFEA dissolved ether oligomers of SEI into the soaking electrolyte, consistent with XPS results. Similarly, SEI treated with LiFEA electrolyte showed a lower intensity of  $\text{CO}_3^-$  than with RCE after its maximum peak, verifying a carbonate-cleaning process induced by LiFEA electrolyte. Visual 3D images further revealed a majority of  $\text{C}_2\text{H}_3\text{O}^-$  and  $\text{CO}_3^-$  signals located in the outer layer of residue SEIs (Fig. 8c) with LiFEA soaking resulting in weaker signals compared to RCE. The lowered signal intensity vividly showed that LiFEA could clean out organic species containing C–O and retain inorganic-rich components in SEI.

Next, we studied the in situ formed SEI to attest whether this self-cleaning concept adapted LiFEA-based electrolytes under a fast-cycling rate (Supplementary Note 6). Although an approximately equivalent C content was observed for SEIs formed in LiFEA electrolytes and RCE, the SEI of LiFEA electrolytes had a C–O content of 26.5%, 15.1% and 16.5% at the sputtering time of 0, 60 and 160 s, respectively, lower than that of RCE (41.0%, 31.6% and 38.5%) (Supplementary Figs. 41 and 42). In O 1s spectra, the decreased C–O content was proven

to be  $\text{Li}_2\text{CO}_3/\text{ROCO}_2\text{Li}$  and  $-(\text{CH}_2\text{CH}_2\text{O})_n^-$  components (Supplementary Fig. 43), agreeing with XPS and TOF-SIMS results of the soaking experiment. By comprehensively examining the high-resolution F 1s and Li 1s spectra (Supplementary Figs. 44 and 45), we observed that LiFEA electrolytes could dissolve the  $\text{Li}_2\text{CO}_3/\text{ROCO}_2\text{Li}$  component detrimental to Li-ion diffusion properties for SEI<sup>9,37,38</sup> and also enrich the inorganics LiF and  $\text{Li}_2\text{O}$ . The content of LiF plus  $\text{Li}_2\text{O}$  reached 73.9%, 82.7% and 66.7% at the sputtering time of 0, 60 and 160 s, respectively; by contrast, RCE maintained a content of 42.4% (0 s), 48.3% (60 s) and 53.5% (160 s). Thus, the LiFEA's cleaning action of unfavourable organic species did facilitate an SEI structure with abundant inorganic components, testifying to the SEI self-cleaning concept induced by LiFEA electrolytes.

As for advanced LiFEA electrolytes, LiFEA served two critical functions: boosting  $\text{LiNO}_3$  solubility in carbonate electrolytes and cleaning undesirable organics in the SEI. The resulting SEI possessed a lower C but higher Li contents than RCE and LiFEA electrolytes (Fig. 8d), indicating that a robust inorganic-rich SEI was successfully established. Due to the cooperation between self-cleaning LiFEA and beneficial  $\text{LiNO}_3$  additive, advanced LiFEA electrolytes promoted SEIs with low signals of organic species, considerably strong  $\text{Li}_2\text{O}$  signals, N-containing reductive products and LiF (Fig. 8d and Supplementary Fig. 46–48), endowing the SEI with an enhanced mechanic property and improved Li-ion diffusion kinetics<sup>39</sup>. It should be noted that adding  $\text{LiNO}_3$  to LiFEA electrolytes could indeed increase  $\text{Li}_2\text{O}$  content to form an inorganic-rich SEI to an extent. Differently, LiFEA in advanced LiFEA electrolytes enabled a robust, inorganic-rich SEI by the behaviour of cleaning out organic species, demonstrated by a lower C–O content at each sputtering depth and an accumulated  $-(\text{CH}_2\text{CH}_2\text{O})_n^-$  at the SEI outer layer compared with RCE (Supplementary Figs. 46, 48 and 49). As expected, advanced LiFEA electrolytes promote uniform Li depositions, reduce SEI's affinity towards organic solvents<sup>3</sup> and suppress the severe Li corrosion issue in carbonate electrolytes at high current densities (Supplementary Figs. 50–54 and Supplementary Note 7). In summary, LiFEA with a pseudo-crown ether-like fold structure had desirable physicochemical properties and a self-cleaning mechanism, thus endowing carbonate-based electrolytes with impressive fast-cycling performances for LMBs.

## Conclusions

In this work, we report a pseudo-crown ether-like functional Li salt, LiFEA, for fast charging/discharging practical LMBs. LiFEA features a large dipole moment, a high DN and a high  $t_{\text{Li}}^+$  in carbonate solvents. It can dissolve undesirable organic species during the SEI construction process in carbonate electrolytes, leading to the gradual enrichment of inorganic species in the SEI. This self-cleaning mechanism facilitates the generation of a dense and uniform inorganic-rich SEI. Our designed carbonate-based electrolytes enabled a high rate capability and long cyclability for the high-voltage LMBs. Practical Li||NCM811 metal pouch cells achieved simultaneous high energy density and power density, enabling a cell-level energy density of  $\sim 310 \text{ Wh kg}^{-1}$  (except taps and packing foil,  $413 \text{ Wh kg}^{-1}$ ) and a power density of  $\sim 410 \text{ W kg}^{-1}$  (except taps and packing foil,  $550 \text{ W kg}^{-1}$ ). Our work demonstrates that by correlating the intramolecular supra-structure of Li salt and its physicochemical properties, such as molecular dipole DN and  $t_{\text{Li}}^+$ , high-quality robust SEI and thereby high-performance batteries can be made with traditional carbonate electrolytes.

## Methods

### Materials

2-[2-(2-Methoxyethoxy)ethoxy]ethylamine and trifluoromethanesulfonic anhydride were purchased from Meryer. Triethylamine and lithium hydride were obtained from Shanghai Titan and Energy-chemical, respectively. Lithium carbonate, lithium fluoride and lithium acetate were purchased from InnoChem Technology. Lithium oxide, lithium

oxalate and poly(ethylene oxide) (Mn: 10,000) were obtained from Macklin Regent, Adamas-beta and Sigma Aldrich, respectively. Dichloromethane (water <50 ppm), acetonitrile (anhydrous) and diethyl ether were purchased from InnoChem or Beijing Lanyi. All chemicals were used as received. Battery-grade lithium salts (that is,  $\text{LiPF}_6$ , LiTFSI,  $\text{LiNO}_3$ ), commercial electrolytes, organic solvents along with NCM811 particles were purchased from Nanjing Mojiesi Energy Technology or DodoChem. 2032-type coin cells with Celgard 2325/25  $\mu\text{m}$  separator were provided by Guangdong Canrd New Energy. Metallic Li was purchased from China Energy Lithium. Industry-level Li||NCM811 pouch cells were purchased from Hunan Li-Fun Technology. The homemade NCM811 cathode sheets were prepared by mixing NCM811 particles, super-P and PVDF with a mass ratio of 8:1:1 and dried under vacuum overnight.

### Syntheses

LiFEA was synthesized by a two-step procedure: sulfonation of amines and deprotonation of the resulting sulfonimides with lithium hydride<sup>40</sup>.

**Synthesis of HFEA.** To a round-bottom flask, 2-[2-(2-methoxyethoxy)ethoxy]ethylamine was first placed and then added 150 ml anhydrous dichloromethane. After stirring the mixture for 30 min, 1.3 equivalent triethylamine was injected into the above solution and followed by transferring the flask into a cooling system (about  $-80^\circ\text{C}$ ). Finally, trifluoromethanesulfonic anhydride (1.01 equivalent) was dropwise added into the cooling mixture and kept stirring for 2 hours. The solvents were removed under vacuum, and the residue was dissolved by concentrated NaOH aqueous, byproducts extracted by dichloromethane and neutralized by hydrochloric acid. The target product was obtained after extracting with dichloromethane and drying under vacuum. Yield: 70%. The corresponding characterization was listed in Supplementary Figs. 55–57.

**Synthesis of LiFEA.** In a 250 ml round-bottom flask, the obtained HFEA was dissolved by anhydrous acetonitrile. The flask was then transferred to an ice water bath and maintained cooling for 30 min. Lithium hydride was slowly added into the mixture under moderate stirring. Four hours later, the ice water bath was removed and kept the reaction for 1 day. During its early stage, more attention was paid to the produced hydrogen gas because of its flammability and explosivity and the increased pressure in the flask. After the reaction ended, the crude product was attained by filtering the suspension and drying the resultant filtrate under a vacuum. The purified LiFEA was crystallized in diethyl ether at a low temperature. Yield: 81%. The corresponding characterization was listed in Supplementary Figs. 1–4.

### Electrolytes

$\text{LiPF}_6$  (152 mg) was dissolved in 1 ml EC/DEC (v/v = 1:1) to obtain the reference carbonate electrolyte of RCE, 1 M  $\text{LiPF}_6$  in EC/DEC (v/v = 1:1). The LiFEA electrolyte was prepared by dissolving LiFEA (30 mg) and  $\text{LiPF}_6$  (152 mg) into 1 ml EC/DEC (v/v = 1:1). For the advanced LiFEA electrolyte,  $\text{LiNO}_3$  additive (7 mg) was dispersed into 0.1 M LiFEA (1 ml) and  $\text{LiPF}_6$  (152 mg) was subsequently added to the above mixture. The control electrolyte (diglyme +  $\text{LiNO}_3$ ) was prepared by dissolving 152 mg  $\text{LiPF}_6$  into a saturated solution of 0.1 M diglyme and  $\text{LiNO}_3$  in EC/DEC (v/v = 1:1). All the electrolytes were prepared inside an argon-filled glovebox ( $\text{O}_2 < 0.1 \text{ ppm}$ ,  $\text{H}_2\text{O} < 0.1 \text{ ppm}$ ) at room temperature.

### Theoretical simulations

The electrostatic potentials (ESPs) and molecular dipoles of LiFEA and LiTFSI were calculated by density-functional theory (DFT) simulation with the Gaussian 16 package. All DFT calculations were conducted at the B3LYP/6-311 + +g(d,p) level. The binding energy between  $\text{Li}^+$  and anion was calculated as the difference between the energy of ion complexes and the energy of isolated ions.

Molecular dynamics (MD) simulations were operated with Gromacs 2021.3. The molar ratios of solvent and lithium salt were set at an experimental condition of 0.1 M LiFEAEC/DEC ( $v/v = 1:1$ ). Molecules and ions were described by the Optimized Potentials for Liquid Simulations All atom force field. Partial charges were determined by fitting molecular ESP obtained in DFT calculations. The simulation boxes were cubic with a side length of about 5.3 nm. The simulations were carried out at 300 K and 1 bar.  $\text{Li}^+$  solvation structures were analysed with Visual Molecular Dynamics.

**Material characterizations.** Nuclear magnetic resonance (NMR) spectra were recorded on a Bruker Avance III HD 400 or JEOL ECS-400 NMR spectrometer. All the NMR samples were measured at room temperature unless otherwise specified. The Li-deposited morphologies under different current densities were characterized by a Zeiss Merlin scanning electron microscope (SEM). The JEM-2100 Plus transmission electron microscope (TEM) at an accelerating voltage of 200 kV was taken to characterize CEI layers coating on cathode NCM811 particles. X-ray photoelectron spectrometer (XPS) was applied to analyse the chemical composition of SEI layers. The XPS spectra were acquired on a Thermo Fisher Scientific ESCALAB Xi, with a sputtering rate of  $30 \text{ nm min}^{-1}$  (calibrated by  $\text{SiO}_2/\text{Si}$ ). To confirm the swept organics in soaked experiments, we analysed the processed SEI layers by TOF-SIMS5 (ION-TOF-GmbH). TOF-SIMS spectra and ion images were collected using  $\text{Bi}^{3+}$  ion beam accelerated at 30 keV and  $\text{Cs}^+$  accelerated at 1 keV. The analysing area was  $100 \mu\text{m} \times 100 \mu\text{m}$  and the sputtering rate was controlled at  $0.19 \text{ nm s}^{-1}$  for  $\text{SO}_2$ . The viscosity was measured using a rotational viscometer (Brookfield, DV-IIa+P). The contact angle between the electrolyte and Celgard 2325 separator was acquired by a tensiometer (Dataphysics Instruments, OCA15EC).

**Quartz crystal microbalance analysis.** Quartz crystal microbalance (QCM) analysis was applied to track the mass variation of a formed SEI layer during immersing in the electrolytes of RCE or LiFEA electrolyte. QCM measurements were conducted by using a QSense Explorer (Biolin Scientific AB) with copper-coated quartz crystal sensor chips (QSX 313, Biolin Scientific AB). The sensor coated with Cu film acted as a working electrode (WE).  $\text{LiFePO}_4$  sheet worked as a counter electrode (CE) and reference electrode (RE), which provided  $\text{Li}^+$  sources for in situ forming a SEI layer on the deposited Li metal. Before QCM measurement, a pristine SEI was generated in RCE by an extra Li electrodeposition process, under a current of 0.05 mA for 30 min.

**Electrochemical measurements.** All the electrochemical tests used a 2032-type coin cell assembled with a Celgard 2325 separator or pouch-cell configurations, which were prepared in the glovebox. The  $\text{Li}^+$  transference number was measured by the Bruce and Vincent method<sup>23</sup>, and the polarization voltage was set at 10 mV for  $\text{Li}||\text{Li}$  cells. Electrochemical impedance spectroscopy was investigated by Princeton electrochemical workstation at a frequency ranging from 0.1 Hz to 100 kHz. The charging/discharging process of coin cells and pouch cells was recorded on a LANHE CT3001A battery testing station at room temperature. For the  $\text{Li}||\text{Cu}$  cells, the diameter of Cu foil and Li metal was controlled at 16 mm and 12 mm, respectively. The  $\text{Li}||\text{NCM811}$  half cells were assembled with  $450 \mu\text{m}$ -thickness Li metals as anode and  $-0.6 \text{ mAh cm}^{-2}$  NCM811 sheets as cathodes. For the NCM811 full cells, a  $40 \mu\text{m}$ -thickness Li foil paired with a high active material mass loading cathode of  $-2.6 \text{ mA cm}^{-2}$ . The  $\text{Li}||\text{NCM811}$  coin and pouch cells were cycled at a constant-current-constant-voltage model. Specifically, the cells were charged to 4.3 V and then kept the voltage until the charging current lowered to 0.1 C (pouch cells, one-half cycling current). Before the cycling tests, all pouch cells proceeded with a two-cycle formation at  $0.366 \text{ mA cm}^{-2}$  (that is, 0.1 C) and degassing. The stack pressure for pouch cells was  $-350 \text{ kPa}$ . Part of the cell design and cycling parameters

were summarized in Supplementary Table 6. The weight of pouch-cell components is listed in Supplementary Table 7.

### Self-cleaning behaviour for SEI layers

We used EC-QCM measurements to investigate the cleaning (dissolving) phenomenon induced by LiFEA, and the pristine SEI layer was constructed in situ in conventional RCE. After in situ replacing the original electrolyte with either fresh RCE or LiFEA electrolyte for soaking treatment, the instrument would record mass changes of the SEI layer, during which some of the formed SEI components would gradually dissolve into the electrolyte. Subsequently, we provided ex situ XPS and TOF-SIMS measurements to confirm those SEI components dissolved by LiFEA electrolytes during soaking. Unlike the in situ EC-QCM experiment, the SEI layers were constructed by cycling  $\text{Li}||\text{Cu}$  cells with RCE under  $3 \text{ mA cm}^{-2}$  (area capacity:  $1 \text{ mAh cm}^{-2}$ ) for ten cycles before soaking. Finally, we studied the in situ formed SEI layer to attest that the self-cleaning mechanism adapted LiFEA-based electrolytes under a fast charging rate. The SEI layers were constructed in LiFEA electrolyte and advanced LiFEA electrolyte using  $\text{Li}||\text{Cu}$  cells at  $3 \text{ mA cm}^{-2}$  (area capacity:  $1 \text{ mAh cm}^{-2}$ ) for ten cycles. The SEI underwent no further soaking treatment.

### Data availability

The datasets analysed and generated during the current study are included in the paper and its Supplementary Information file. Source data are provided with this paper.

### References

- Niu, C. et al. Self-smoothing anode for achieving high-energy lithium metal batteries under realistic conditions. *Nat. Nanotechnol.* **14**, 594–601 (2019).
- Holoubek, J. et al. Tailoring electrolyte solvation for Li metal batteries cycled at ultra-low temperature. *Nat. Energy* **6**, 303–313 (2021).
- Zhang, Z. et al. Capturing the swelling of solid-electrolyte interphase in lithium metal batteries. *Science* **375**, 66–70 (2022).
- Xiao, J. et al. Understanding and applying Coulombic efficiency in lithium metal batteries. *Nat. Energy* **5**, 561–568 (2020).
- Kim, M. S. et al. Suspension electrolyte with modified  $\text{Li}^+$  solvation environment for lithium metal batteries. *Nat. Mater.* **21**, 445–454 (2022).
- Cheng, X.-B., Zhang, R., Zhao, C.-Z. & Zhang, Q. Toward safe lithium metal anode in rechargeable batteries: a review. *Chem. Rev.* **117**, 10403–10473 (2017).
- Liu, Y. et al. Self-assembled monolayers direct a LiF-rich interphase toward long-life lithium metal batteries. *Science* **375**, 739–745 (2022).
- Fan, X. et al. Non-flammable electrolyte enables Li-metal batteries with aggressive cathode chemistries. *Nat. Nanotechnol.* **13**, 715–722 (2018).
- Zhang, X.-Q. et al. Regulating anions in the solvation sheath of lithium ions for stable lithium metal batteries. *ACS Energy Lett.* **4**, 411–416 (2019).
- Zheng, J. et al. Electrolyte additive enabled fast charging and stable cycling lithium metal batteries. *Nat. Energy* **2**, 17012 (2017).
- Zhou, P. et al. Rationally designed fluorinated amide additive enables the stable operation of lithium metal batteries by regulating the interfacial chemistry. *Nano Lett.* **22**, 5936–5943 (2022).
- Wang, H. et al. Dual-solvent Li-ion solvation enables high-performance Li-metal batteries. *Adv. Mater.* **33**, 2008619 (2021).
- Su, C. C. et al. Solvation rule for solid-electrolyte interphase enabler in lithium-metal batteries. *Angew. Chem. Int. Ed.* **59**, 18229–18233 (2020).



14. Zhang, W. et al. Engineering a passivating electric double layer for high performance lithium metal batteries. *Nat. Commun.* **13**, 2029 (2022).
15. Dong, H. et al. A thermoresponsive composite separator loaded with paraffin@SiO<sub>2</sub> microparticles for safe and stable lithium batteries. *J. Energy Chem.* **62**, 423–430 (2021).
16. Rustomji Cyrus, S. et al. Liquefied gas electrolytes for electrochemical energy storage devices. *Science* **356**, eaal4263 (2017).
17. Yamada, Y. et al. Advances and issues in developing salt-concentrated battery electrolytes. *Nat. Energy* **4**, 269–280 (2019).
18. Ren, X. et al. Enabling high-voltage lithium-metal batteries under practical conditions. *Joule* **3**, 1662–1676 (2019).
19. Fan, X. et al. Highly fluorinated interphases enable high-voltage Li-metal batteries. *Chem* **4**, 174–185 (2018).
20. Qiao, L. et al. Stable non-corrosive sulfonimide salt for 4-V-class lithium metal batteries. *Nat. Mater.* **21**, 455–462 (2022).
21. Amanchukwu, C. V. et al. A new class of ionically conducting fluorinated ether electrolytes with high electrochemical stability. *J. Am. Chem. Soc.* **142**, 7393–7403 (2020).
22. Xue, W. et al. Ultra-high-voltage Ni-rich layered cathodes in practical Li metal batteries enabled by a sulfonamide-based electrolyte. *Nat. Energy* **6**, 495–505 (2021).
23. Diederichsen, K. M., McShane, E. J. & McCloskey, B. D. Promising routes to a high Li<sup>+</sup> transference number electrolyte for lithium ion batteries. *ACS Energy Lett.* **2**, 2563–2575 (2017).
24. Liu, Y., Zhu, Y. & Cui, Y. Challenges and opportunities towards fast-charging battery materials. *Nat. Energy* **4**, 540–550 (2019).
25. Kakiuchi, F. et al. Ruthenium-catalyzed functionalization of aryl carbon–oxygen bonds in aromatic ethers with organoboron compounds. *J. Am. Chem. Soc.* **126**, 2706–2707 (2004).
26. Xu, K. Nonaqueous liquid electrolytes for lithium-based rechargeable batteries. *Chem. Rev.* **104**, 4303–4418 (2004).
27. Nakatsuji, Y. et al. Molecular design of the electron-donating sidearm of lariat ethers: effective coordination of the quinoline moiety in complexation toward alkali-metal cations. *J. Am. Chem. Soc.* **110**, 531–538 (1988).
28. Baxter, N. J. & Williamson, M. P. Temperature dependence of <sup>1</sup>H chemical shifts in proteins. *J. Biomol. NMR* **9**, 359–369 (1997).
29. Gutmann, V. & Wyck, E. Coordination reactions in non aqueous solutions—the role of the donor strength. *Inorg. Nucl. Chem. Lett.* **2**, 257–260 (1966).
30. Schmeisser, M. et al. Gutmann donor and acceptor numbers for ionic liquids. *Chem. Eur. J.* **18**, 10969–10982 (2012).
31. Johnson, L. et al. The role of LiO<sub>2</sub> solubility in O<sub>2</sub> reduction in aprotic solvents and its consequences for Li–O<sub>2</sub> batteries. *Nat. Chem.* **6**, 1091–1099 (2014).
32. Baek, M., Shin, H., Char, K. & Choi, J. W. New high donor electrolyte for lithium–sulfur batteries. *Adv. Mater.* **32**, 2005022 (2020).
33. Kwon, H., Baek, J. & Kim, H.-T. Building lithium metal batteries under lean electrolyte conditions: challenges and progress. *Energy Storage Mater.* **55**, 708–726 (2023).
34. Li, S. et al. A robust all-organic protective layer towards ultrahigh-rate and large-capacity Li metal anodes. *Nat. Nanotechnol.* **17**, 613–621 (2022).
35. Ji, Y. et al. From bulk to interface: electrochemical phenomena and mechanism studies in batteries via electrochemical quartz crystal microbalance. *Chem. Soc. Rev.* **50**, 10743–10763 (2021).
36. Jin, C. et al. Rejuvenating dead lithium supply in lithium metal anodes by iodine redox. *Nat. Energy* **6**, 378–387 (2021).
37. Choudhury, S. et al. Designing solid-liquid interphases for sodium batteries. *Nat. Commun.* **8**, 898 (2017).
38. Biswal, P. et al. A reaction-dissolution strategy for designing solid electrolyte interphases with stable energetics for lithium metal anodes. *Cell Rep. Phys. Sci.* **3**, 100948 (2022).
39. Liu, S. et al. An inorganic-rich solid electrolyte interphase for advanced lithium-metal batteries in carbonate electrolytes. *Angew. Chem. Int. Ed.* **60**, 3661–3671 (2021).
40. Dillon, R. E. A. & Shriver, D. F. Thermal and complex impedance analysis of amorphous and crystalline lithium salt mixtures. *Solid State Ionics* **140**, 375–380 (2001).

## Acknowledgements

This work was supported by the National Nature Science Fund of China (grant number 22071133, K. L.), Beijing Natural Science Foundation (grant number Z220020, K.L.), Recruitment Program of Guangdong (grant number 2016ZT06C322, X.K.), China Postdoctoral Science Foundation (grant number 2021M701872, Y.X.) and TCL Science and Technology Innovation Fund (X.K.). We thank C. Guo and Z. Li from Analysis Center, Tsinghua University for analysing the TOF-SIMS data, Y. Li from State Key Laboratory of Space Power-Sources Technology, Shanghai Institute of Space Power Sources for helpful discussion and C. Cui from Chemistry and Chemical Engineering, Hunan University for discussing electrochemical measurements. We thank J. Fang (Tsinghua University) and Biolin Scientific AB for QCM experiments and data analysis.

## Author contributions

Y.X. and K.L. conceived the idea and designed the experiments. Y.X., P.Z., X.K., J.T., W.Z., S.Y., W.-h.H., H.-Y.Z., Z.X. and L.W. carried out the experiments and measurements. H.D., X.C., P.W. and B.W. helped with discussion. Y.X., X.K. and K.L. analysed the data and prepared the manuscript with contributions from all authors.

## Competing interests

For K. Liu and Y. Xia, this work has been filed as a China invention patent, patent number CN113871718B. The other authors declare no competing interests.

## Additional information

**Supplementary information** The online version contains supplementary material available at <https://doi.org/10.1038/s41560-023-01282-z>.

**Correspondence and requests for materials** should be addressed to Kai Liu.

**Peer review information** *Nature Energy* thanks Hee-Tak Kim, Yuki Yamada and the other, anonymous, reviewer(s) for their contribution to the peer review of this work.

**Reprints and permissions information** is available at [www.nature.com/reprints](http://www.nature.com/reprints).

**Publisher's note** Springer Nature remains neutral with regard to jurisdictional claims in published maps and institutional affiliations.

Springer Nature or its licensor (e.g. a society or other partner) holds exclusive rights to this article under a publishing agreement with the author(s) or other rightsholder(s); author self-archiving of the accepted manuscript version of this article is solely governed by the terms of such publishing agreement and applicable law.

© The Author(s), under exclusive licence to Springer Nature Limited 2023